Ceramics International 43 (2017) 5759–5766

Contents lists available at ScienceDirect

Ceramics International

journal homepage: www.elsevier.com/locate/ceramint

Blue and red light photoluminescence emission at room temperature from $CaTiO_3$ decorated with α-Ag_2WO_4

Mayara Mondego[a,*], Regiane C. de Oliveira[a], Maya Penha[a], Máximo Siu Li[b,c], Elson Longo[a,c]

[a] CDMF-UFSCar, Universidade Federal de São Carlos, P.O. Box 676, 13565-905 São Carlos, SP, Brazil
[b] IFSC, Universidade de São Paulo, P.O. Box 369, 13560-970 São Carlos, SP, Brazil
[c] CDMF-UNESP, Universidade Estadual Paulista, P.O. Box 355, 14801-907 Araraquara, SP, Brazil

ARTICLE INFO

Keywords:
Optical properties
Decoration
Calcium titanate
Silver tungstate

ABSTRACT

$CaTiO_3$ (CT) and α-Ag_2WO_4 (AW) semiconductors are widely known for their interesting electrical and photoluminescence (PL) properties. In this study, we decorated CT with AW for obtaining $CaTiO_3$:α-Ag_2WO_4 (CT:AW), and investigated the properties of the produced materials, especially their PL properties. The X-ray diffraction peaks of the synthesized microcrystals were well indexed to the orthorhombic phase for all the samples. Two morphologies: cube-like for CT and rod-like for AW were observed by field-emission scanning electron microscopy (FE-SEM). The FE-SEM and transmission electron microscopy (TEM) studies indicated the presence of rod-shaped AW deposited on the surfaces of cube-shaped CT morphology. PL emission of the decorated samples overlaps all the visible region spectra because of the contribution from both the constituent materials that induce maximum emissions in the blue and red regions. The examination of *Commission internationale de Íéclairage* (CIE) coordinates confirmed that the decorated samples exhibit favored emission the red wavelength region.

1. Introduction

Technological applications of semiconductor materials have stimulated the research for improving or modulating their properties [1–3]. Recently, semiconductors exhibiting photoluminescence (PL) properties have received significant attention owing to their applications in several devices such as light emitting diodes (LEDs), displays, and optical markers [4]. Among the various semiconductor materials exhibiting PL properties, $CaTiO_3$ (CT) and α-Ag_2WO_4 (AW) have received a special attention [5–8].

CT is a perovskite material that exhibits PL properties in both semi-ordered and amorphous forms [9–11]. CT is present in four structurally stable forms: cubic, monoclinic, tetragonal, and orthorhombic phases [12]. Orthorhombic CT exhibits PL at room temperature, which is associated with the structural organization of the material. This organization depends on the method of synthesis, time, and heat treatment temperature (if any) of the material since these parameters influence its structural organization [13,14]. PL properties of CT can be attributed to the lattice defects such as oxygen vacancies. These defects modify the coordination of titanium and calcium atoms, thereby affecting the PL properties [15–17].

Moreira et al. [18] synthesized CT using a microwave-assisted hydrothermal (MAH) method by varying the synthesis time from 10 to 160 min. PL properties of the obtained powders were examined at room temperature using an excitation wavelength of 350.7 nm. A broadband profile was observed that was attributed to the presence of intermediate energy states within the band gap; the intrinsic defects present in the material were responsible for the energy states.

The semiconductor material, AW, exists in three structural forms, α-orthorhombic, β-hexagonal, and γ-cubic phases, depending on the reaction conditions (temperature and pH) employed in the synthesis [19]. The properties of AW are known to depend on the interactions between the octahedral clusters of $[WO_6]$ and $[AgO_x]$ (x=2, 4, 6, and 7) [20]. Lin et al. [21] examined the PL properties of AW and concluded that the PL emissions could be attributed to the charge transfer occurring from the distorted $[WO_6]$ clusters to the undistorted $[WO_6]$ clusters.

Considering the interesting PL proprieties of CT and AW semiconductors, we aimed at combining both the materials in order to prepare an advanced material that can exhibit features resulting from the formation of the decorated. AW was synthesized using a coprecipitation (CP) method with a mixture of saturated solutions of the soluble precursor reagent. This low-cost method is simple and uses a low reaction temperature, good homogeneity and uniform-sized particles [22]. CT was synthesized by the MAH method, a high-energy

* Corresponding author.
E-mail address: mayaramondego.ufma@gmail.com (M. Mondego).

http://dx.doi.org/10.1016/j.ceramint.2017.01.121
Received 5 October 2016; Received in revised form 28 December 2016; Accepted 24 January 2017
Available online 25 January 2017

method, which has received attention as it offers significant advantages: environmentally-friendly conditions, relatively low processing temperature, and short reaction time, over the conventional methods [14,23,24]. A simple mixing of CT and AW was carried out for preparing decorated CT:AW samples.

The obtained powders were characterized using X-ray diffraction (XRD), Raman spectroscopy, field-emission scanning electron microscopy (FE-SEM), and transmission electron microscopy (TEM). Ultraviolet-visible (UV–vis) absorption and PL spectroscopy measurements were carried out at room temperature in order to examine the correlation between the optical properties and the structural order-disorder effects caused by the interaction between CT and AW.

2. Experimental procedures

2.1. Synthesis of $CaTiO_3$

The CT microparticles were prepared by modifying a method reported by Mazzo et al. [25]. Initially, calcium chloride, 0.01 mol of $CaCl_2{\cdot}2H_2O$ (99.0%, Sigma-Aldrich) was dissolved in 50 mL distillated water in a Teflon autoclave under stirring with a continuous flow of N_2. After 5 min, 0.01 mol of titanium isopropoxide, $Ti(OC_3H_7)_4$ (97%, Sigma-Aldrich) was added in solution and stirred for 20 min 50 mL KOH (6 M) solution was then added to this solution in order to act as the mineralizer. The precipitate formed was then processed by the MAH method, by heating at 140 °C for different times (4, 8, 16, and 32 min). The powders were cooled to room temperature, centrifuged, and washed with distilled water until a neutral pH was achieved followed by drying the product in a conventional furnace at 60 °C for 12 h.

2.2. Synthesis of α-Ag_2WO_4

The AW sample was prepared according to the method reported by Santana et al. [26]. The AW was previously prepared using nitric acid aqueous solution with pH 4 (HNO_3, 65.0%, Synth). Initially, 1 mmol $Na_2WO_4{\cdot}2H_2O$ (99.5%, Sigma-Aldrich) and 2 mmol $AgNO_3$ (99.0%, Synth) were separately dissolved in 25 mL solution with pH 4 under stirring. The precursor solutions were heated at 70 °C and mixed. The precipitate formed was washed and dried in a conventional furnace at 60 °C for 24 h.

2.3. Synthesis of α-Ag_2WO_4 decorated $CaTiO_3$

0.2340g of the prepared AW sample was dispersed in 25 mL distillated water by ultrasonic agitation carried out for 15 min 0.4386g of the prepared CT samples at different times (4, 8, 16, and 32 min) obtained in Section 2.1 were separately dispersed in 25 mL distillated water for 5 min using an ultrasonic processor (pulse on 3 s and pulse off 2 s). The ultrasonic treatment was carried out in order to enhance the dispersion of the CT powders. For decoration, each CT solution was then added to the AW solution under vigorous stirring, and the mixture was stirred for 10 min at room temperature. The powder samples were centrifuged, washed with distilled water, and dried in a conventional furnace at 35 °C for 24 h. This decoration step was employed for all the CT powder samples obtained with different times and denoted as CT:AW4, CT:AW8, CT:AW16, and CT:AW32, corresponding to the CT samples prepared in 4, 8, 16, and 32 min, respectively.

2.4. Characterization

The obtained samples were characterized by XRD using a Rigaku DMax 2500PC (Japan) diffractometer with Cu-Kα (λ=1.5406 Å) radiation in the 2θ range of 10–80° with a scanning speed of 2°/min. Raman spectroscopy scattering measurements were performed using an iHR550 Horiba Jobin-Yvon (Japan) coupled to a CCD detector. The spectra were obtained in the range of 30–1000 cm^{-1} using argon ion laser having a wavelength of 514.5 nm with a maximum power of 200 mW. UV–vis spectroscopic measurements were performed using a Cary 5G (Varian, USA) spectrophotometer in diffuse reflection mode. The morphological features of the obtained materials were examined using FE-SEM with a Supra 35-VP Carl Zeiss (Germany) operating with an accelerating voltage of 5 kV and TEM with a FEI microscope model Tecnai G2F20 operating at 200 kV. PL spectra were collected using a Monospec 27 monochromator Thermal Jarrel Ash coupled to R955 photomultiplier (Hamamatsu Photonics, Japan). A krypton ion laser (Coherent Innova 200 K; λ=350 nm) was used as the excitation source with a maximum output power of 500 mW, and the measurements were performed at room temperature.

3. Results and discussion

The long-range structural order, periodicity, as well as the structural phase of the material were evaluated by analyzing the XRD peaks. Fig. 1(a) shows the XRD patterns of the CT powders treated for different times (4, 8, 16, and 32 min) at 140 °C by the MAH method. All the diffraction peaks could be indexed to the orthorhombic phase with a space group of *Pbnm* according to the Joint Committee on Powder Diffraction Standards (JCPDS) card No. 42-0423 [27]. The 4, 8, and 16 min samples exhibit a *halo* in the baseline, located between 20° and 40 °, indicating the presence of an amorphous phase in the samples. However, with an increase in the synthesis time, the crystallinity of the samples improved, resulting in a decrease in this *halo*. Hence, CT exhibits a long-range disorganization, which decreases with an increase in the synthesis time.

In order to confirm the short-range organization of the material, Raman measurements were carried out, and the results are presented in Fig. 1(b). The observed Raman-active vibration modes confirm the orthorhombic phase of all the samples [28].

The peak observed at 123 cm^{-1} could be attributed to the Ca-TiO_3 lattice mode. The peaks located at 178, 221, 243, 285, and 339 cm^{-1} are assigned to the O-Ti-O bending modes. The peaks detected at 461 and 540 cm^{-1} are attributed to the torsional vibration in TiO_3, and the peak at 685 cm^{-1} is assigned to the Ti-O symmetric stretching vibration [29,30]. A broadband is observed in the range of 600–750 cm^{-1} in the Raman spectra of all the CT samples. However, in the case of the CT sample obtained with a synthesis time of 4 min, two small peaks (two horizontal arrows) are observed in the 600–750 cm^{-1} range, suggesting the presence of two titanium clusters [TiO_5] and [TiO_6] in the sample [14].

Thus, some of the Raman peaks are not well defined in the case of the 4 and 8 min CT samples, indicating the short-range structural disorder present in the samples. The Raman spectra obtained for the 16 and 32 min CT samples exhibit more well-defined peaks, indicating a possible decrease in the defects and an increase in the crystallinity of the sample [31]. Moreover, all the CT samples exhibit a peak in the 800–900 cm^{-1} range, suggesting a cation order-disorder, which is more evident in the 4 and 8 min CT samples [32]. Thus, all the CT samples treated for different times at 140 °C using the MAH method exhibit a low short-range organization due to a degree of the structural order-disorder.

The morphology of the CT samples reflects their structural organization and (the FE-SEM images are shown in Fig. 1(c). The CT sample prepared using a synthesis time of 4 min by the MAH process consists of micro-cubes with edge lengths in the order of 3.3 ± 0.1 μm. It can be seen amorphous parts in the sample which is formed by aggregate of particles that were nucleation process and self-assembly. With a synthesis time of 8 min, a sample consisting of micro-cubes with edge lengths in the order of 4.3 ± 0.1 μm as well as amorphous particles is obtained. Increasing the synthesis time to 16 and 32 min favors the formation of rectangular bars with a flat surface. The CT sample

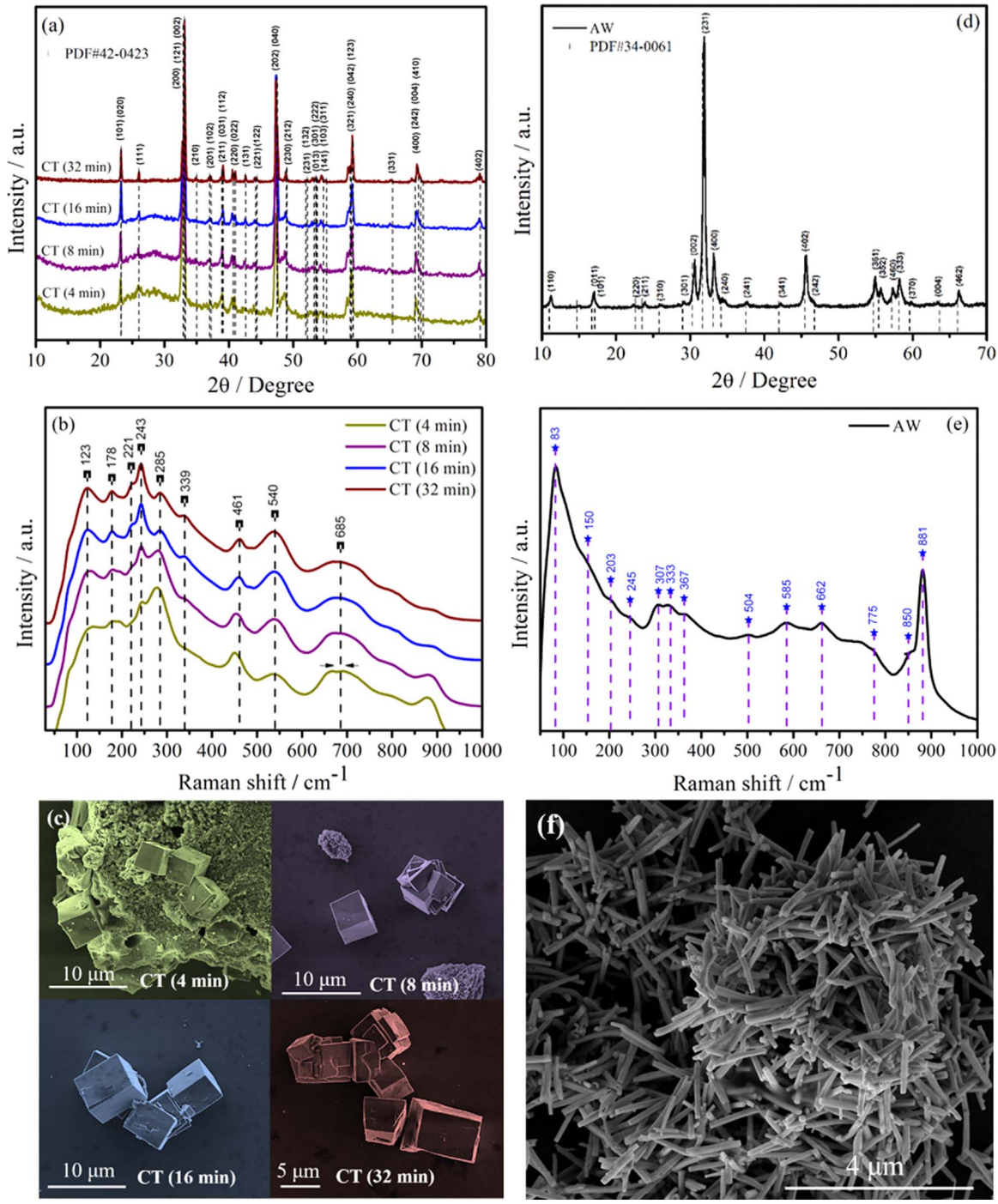

Fig. 1. Structural and morphological characterization for the CT and AW samples. (a) XRD patterns of the CT samples. (b) Raman spectra of CT samples. (c) FE-SEM images of CT samples. (d) XRD pattern of the AW. (e) Raman spectrum of the AW. (f) FE-SEM images of AW.

synthesized with 16 min consists of edges with lengths in the order of 5.0 ± 0.8 μm. For the 32 min CT sample presents lengths of 5 ± 1 μm, a variation in the size is not observed. Thus, the growth and organization of particles enhanced with an increase in the synthesis time, as observed with the XRD and Raman examinations.

For the AW sample obtained by the CP method, intense and well-defined peaks are observed in the XRD pattern, indicating their crystallinity and long-range structural order (Fig. 1(d)). The peaks can be indexed to the orthorhombic phase with a space group of *Pn2n* and a point-group of symmetry of C_{2v}^{10}, in agreement with the JCPDS card No. 34–61 [33].

The Raman spectrum of the AW sample exhibits 13 active modes, which could be assigned to the point-group symmetry of C_{2v}^{10} (Fig. 1(e)). The band observed at 881 cm^{-1} corresponds to the symmetric stretching mode of $[WO_6]$ clusters. The peaks observed between 500 and 50 cm^{-1} can be assigned to the external vibrational modes of $[AgO_x]$ (x=7, 6, 4, and 2) clusters [8, 34, 35]. The modes are not well defined, indicating the short-range structural disorder present in the sample.

The morphology and the microstructure of the AW sample were investigated by examining their FE-SEM images. The FE-SEM image of the AW crystals indicates the presence of uniform rod-like morphology with an average length of 1.0 ± 0.2 μm and a diameter of 0.14 ± 0.2 μm (Fig. 1(f)).

The XRD patterns of the decorated samples are shown in Fig. 2(a).

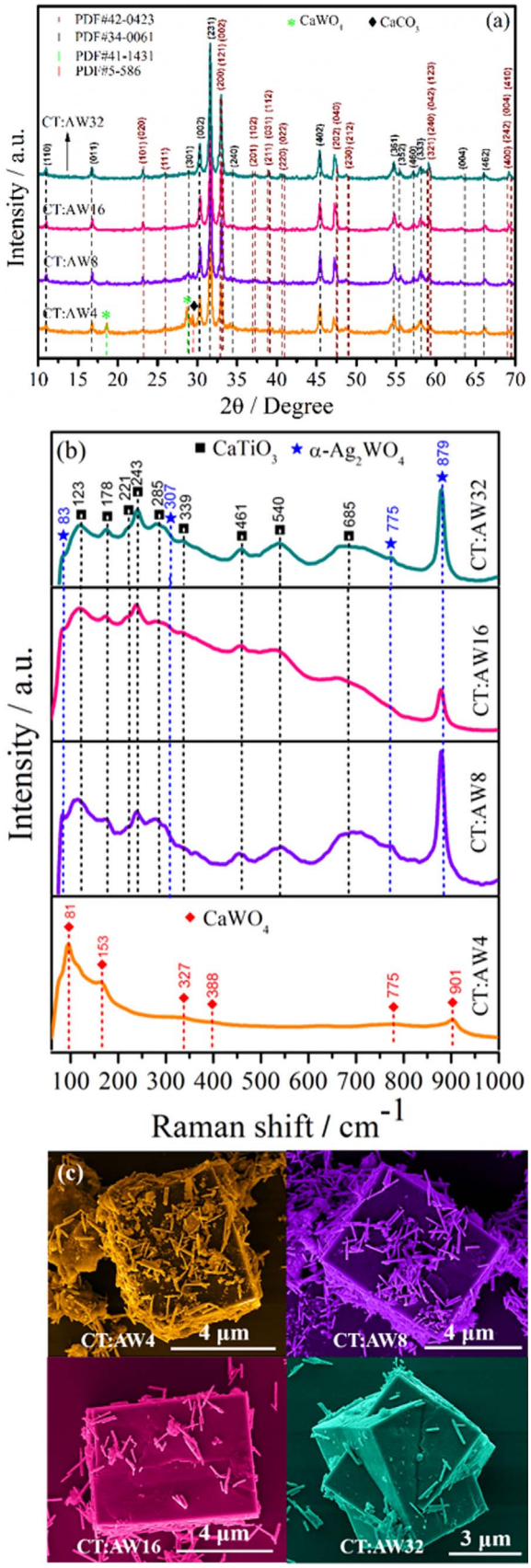

Fig. 2. Structural and morphological characterization of the decorated samples. (a) XRD patterns. (b) Raman spectra. (c) FE-SEM images.

The CT and AW phases coexist in the sample with the patterns of the two phases overlapping. No significant changes in the patterns could be observed at the long range. However, the CT:AW4 and CT:AW8 samples exhibit additional peaks at 18.6° and 28.7°, which could be associated to the presence of $CaWO_4$ as the additional phase, according to the JCPDS card No. 41-1431 [36]. $CaCO_3$ is also present in the sample as evidenced by the peak observed at 29.5° that could be indexed according to JCPDS card No. 5-586. The amorphous phase is observed in higher amounts in the CT sample than that observed in the CT:AW16 and CT:AW32 samples, probably favoring the formation of the $CaWO_4$ and $CaCO_3$ phases. These phases serve as an interface between CT and AW, thereby changing the properties of the samples.

Short-range modifications can be observed from the Raman spectra of the samples (Fig. 2(b)). The CT:AW4 sample exhibits six Raman-active vibrational modes typical of the $CaWO_4$ crystal with two external vibration modes associated with CaO_8, observed at 81 cm^{-1} corresponding to the bending mode (B_g) and at 153 cm^{-1} corresponding to the stretching mode (E_g). Four modes associated with vibrations in the [WO_4] cluster are observed at 327, 388, 775, and 901 cm^{-1}, which correspond to the A_g + B_g bending mode, B_g bending mode, E_g as-stretching mode, and A_g stretching mode [37].

However, the Raman spectra of the CT:AW samples (8, 16, and 32 min) exhibit peaks corresponding to only CT and AW. A large change can be observed in the peaks observed for the decorated samples due to the structural order-disorder effects occurring at the interfacial region. The surface interaction between CT and AW in the decorated sample results in distortion in the short-range structural order in the [TiO_6] clusters. However, some of the vibrational modes of AW cannot be observed in the decorated samples, probably because the intensity of the CT modes is much higher than that of the AW vibrational modes.

Fig. 2(c) shows the FE-SEM images of the decorated samples. The images reveal the presence of hexagonal rod-shaped AW deposited on the surface of the CT cubes, resulting in the formation of the decorated sample (CT:AW). In the case of the CT:AW4 sample, besides the observed cubic CT and rod-like AW morphologies observed, an additional morphology can be seen, which could be associated to $CaWO_4$, since additional peaks are observed in the XRD patterns of this sample, more information about $CaWO_4$ morphology are provided in Supporting Information.

The FE-SEM images of CT:AW samples (8, 16, and 32 min) indicate the presence of two morphological forms corresponding to CT and AW. The AW rods attaches more efficiently on the surface of the cubes formed with a synthesis time of 4 and 8 min. According the surface of the CT cubes become flat and defined, the adhesion between the AW particles is reduced.

The contact area between the CT and AW particles in the CT:AW4 decorated sample is illustrated in the TEM images recorded with different magnifications (Fig. 3). Aggregated AW rod-like particles surrounding the CT cube are observed in the low-magnification image (Fig. 3(a)).

The junction between the CT and AW interface (Fig. 3(b)) indicates a strong interaction between the two materials, favoring the formation of $CaWO_4$, as observed from the XRD and Raman examination results.

3.1. UV–vis diffused reflectance spectroscopy

The experimental optical band gap energy (E_{gap}) values for the CT samples synthesized with different times (4, 8, 16, and 32 min) at 140 °C are presented in Fig. 4. The E_{gap} for the samples were calculated using the Kubelka-Munk and Wood-Tauc equations [38,39].

The CT samples obtained using different synthesis times absorb photons in the wavelength range of 336–343 nm. An increase in the synthesis time does not cause a significant change in the E_{gap} values. However, the obtained E_{gap} values are lower than the corresponding theoretical values reported in the literature (3.98 eV) for the CT sample

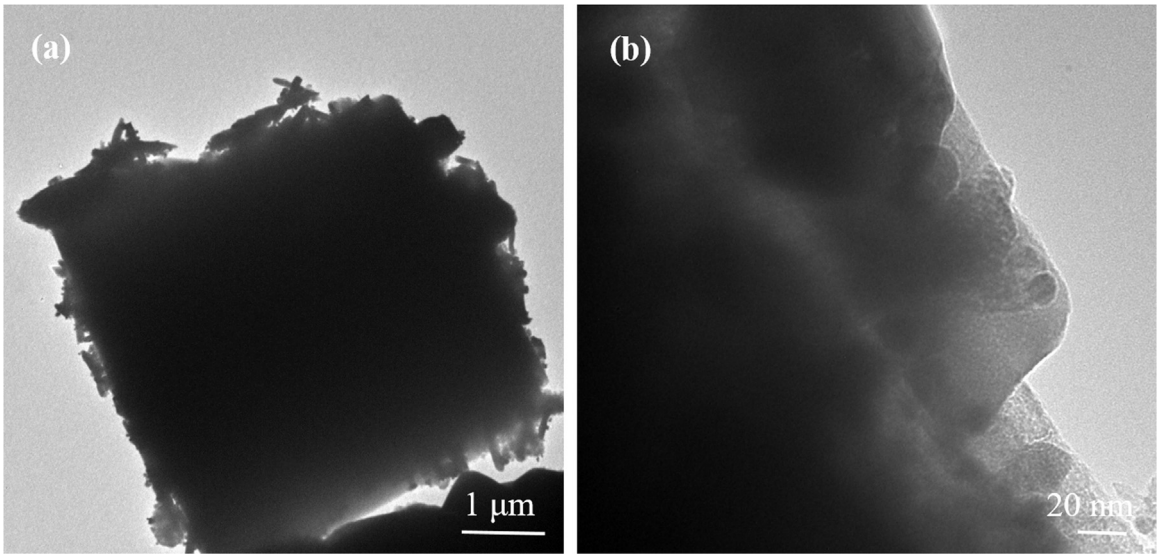

Fig. 3. TEM images of the CT:AW4 decorated. (a) Low magnification and (b) high magnification.

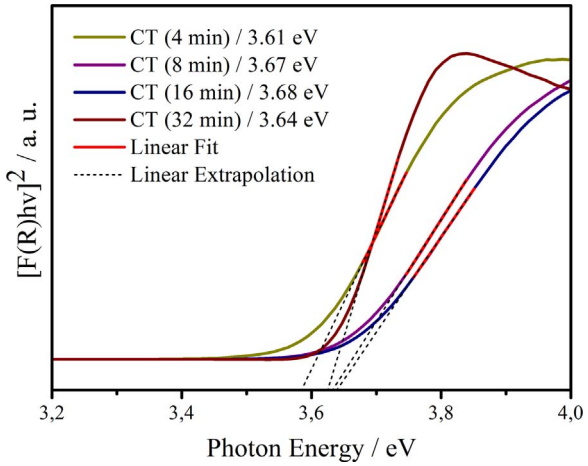

Fig. 4. UV–vis diffused reflectance spectroscopy of CT samples synthesized by the MAH method at 140 °C with variation times.

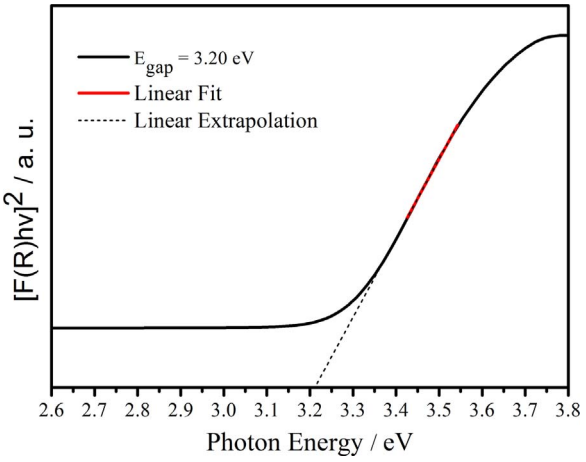

Fig. 5. UV–vis diffused reflectance spectroscopy of the AW synthesized by CP method.

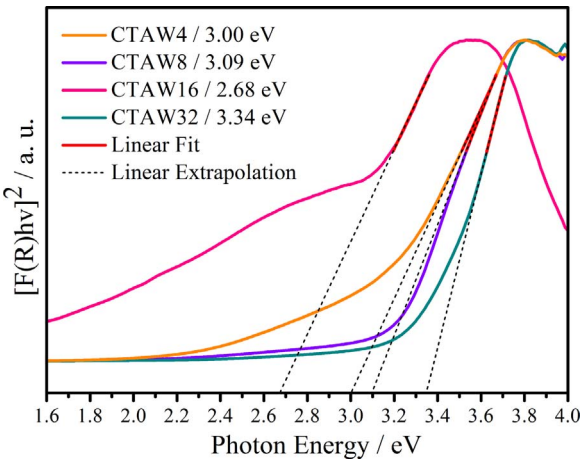

Fig. 6. UV–vis diffused reflectance spectroscopy of the CT:AW decorated samples.

obtained by the MAH method [18]. The changes in the experimental and theoretical E_{gap} values could be attributed to the presence of structural order-disorder in the material that depends on the synthesis time.

The experimental E_{gap} value obtained for AW is 3.20 eV that corresponds to the absorption of photons in the wavelength of 387.5 nm (Fig. 5). The E_{gap} value is less than the corresponding theoretically calculated (3.55 eV) value reported earlier [8]. The decrease in the E_{gap} value could be attributed to the intermediate-range distortions in the sample caused by the presence of the structural and surface defects [40].

The E_{gap} values of the decorated samples are shown in Fig. 6. The band gap values of CT:AW4, CT:AW8, CT:AW16, and CT: AW32 are ~3.00, 3.09, 2.68, and 3.34 eV, respectively, corresponding to the absorption onset edge observed at 413.3, 401.3, 462.7, and 371.3 nm, respectively. A strong absorption occurs in the UV region for blue visible light wavelengths.

3.2. PL

Fig. 7 illustrates the PL spectra recorded with an excitation wavelength of 350 nm for the CT samples synthesized by the MAH method with different times. The excitation spectra monitoring the maximum emission bands of the CT samples are presented in Fig. S3.

All the CT samples exhibit a broadband profile corresponding to a multi-photon process. The 4, 16, and 32 min CT samples exhibit the maximum PL emission in the blue region, and the 8 min CT sample exhibits the maximum PL emission in the orange region (605 nm).

Using the Voigt Area G/L function, the PL curve of the CT samples was deconvoluted to four components at 445 nm (blue), 493 nm

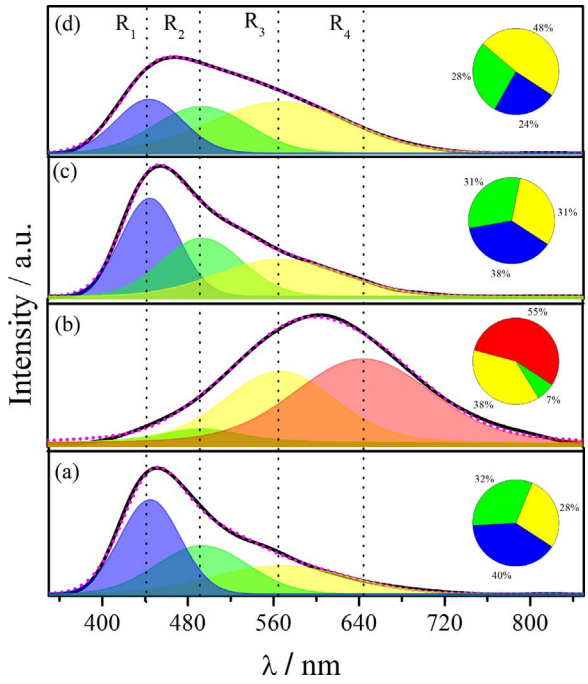

Fig. 7. PL spectra, deconvolution and percentage of color area of CT samples synthesized by the MAH method at 140 °C for (a) 4, (b) 8, (c) 16 and (d) 32 min. (For interpretation of the references to color in this figure legend, the reader is referred to the web version of this article.)

(green), 567 nm (yellow), and 645 nm (red) (Fig. 7), corresponding to the electronic transition occurring at 2.79 eV, 2.51 eV, 2.19 eV, and 1.92 eV, respectively. The electronic transition values indicate that the PL emission occurs because of the participation of various electronic states within the band gap. These electronic states are formed as a result of the various relaxation processes [18] since the E_{gap} experimental values of the CT samples are higher. There is a trapping electron favoring an emission in the blue region, corresponding to the shallow defects located near the conduction and valence bands for the 4, 16, and 32 min CT samples. These defects are caused by breaking of the symmetry processes in the $[TiO_x]$ and $[CaO_{12}]$ clusters [41].

The PL spectrum of the 8 min CT sample synthesized exhibits a new peak in the red region, which is associated with the deep levels within the band gap and is caused by O vacancies. By increasing the synthesis time, samples exhibiting different PL profiles are obtained, consequently achieving emissions in the blue, green, yellow, and red regions.

The PL curve of AW indicates a broadband profile, which is associated to the multi-photon process (Fig. 8) and the excitation spectra monitored by the maximum values of the emission (460, 595, 781 nm) were exhibited in Fig. S4. The PL curve was deconvoluted using the Voigt Area G/L function to four individual components at 450 nm (blue), 555 nm (green), 676 nm (red), and 783 nm (infrared).

AW is known to be composed of $[WO_6]$ and $[AgO_x]$ (x=2, 4, 6, and 7) clusters. The presence of shallow defects, the deformation in the Ag-O and W-O bonds, and the polarization in the lattice lead to the formation of $[WO_6]'/[WO_6]^{\bullet}$ or $[AgO_x]'/[AgO_x]^{\bullet}$ clusters. These distorted clusters cause the occurrence of more energetic emissions in the blue light region, as evidenced from the peaks observed at 450 and 555 nm. Defects such as Ag and O vacancies present in the $[AgO_x]$ and $[WO_6]$ clusters, classified as deep defects and less energetics, cause emissions in the red region, which can be associated to the peaks observed at 676 and 783 nm [21, 42, 43].

Fig. 9 shows the PL spectra of the CT:AW samples and Fig. S5 exhibited PL excitation spectra under maximum emission at 450 and 675 nm. A broadband is observed in the visible region with two maximum emissions centered at 450 nm (blue region) and 675 nm (red region). The emission in the blue region corresponds to the

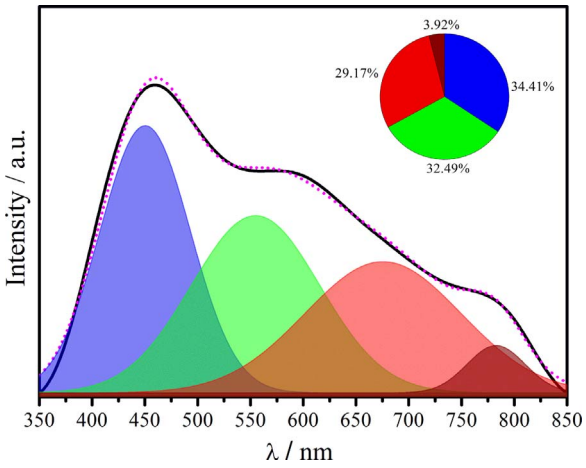

Fig. 8. PL spectrum, deconvolution and percentage of color area of the AW synthesized by CP method. (For interpretation of the references to color in this figure legend, the reader is referred to the web version of this article.)

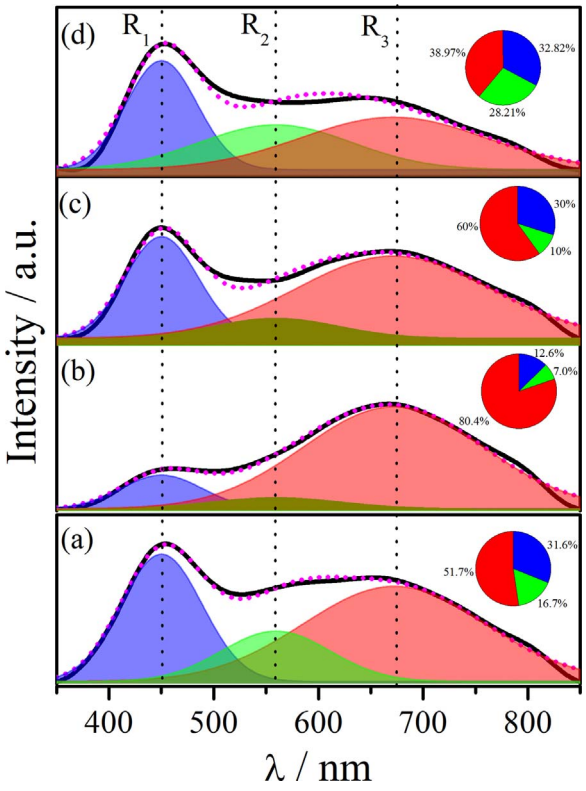

Fig. 9. PL spectra, deconvolution and percentage of color area of the decorated samples (a) CT:AW4, (b) CT:AW8, (c) CT:AW16 and (d) CT:AW32. (For interpretation of the references to color in this figure legend, the reader is referred to the web version of this article.)

distortions present in the clusters of the two materials, and this emission is observed in pure CT and AW. Furthermore, the interaction between AW and CT causes short-range distortions in the $[TiO_6]$ clusters, due to an increase in the Ti-O bonding distance as well as the possible O vacancies present. The generated structural defects might cause the formation of various states in the band gap, which act as carrier recombination centers favoring the PL emission in the red region.

The deconvolution of the PL spectra of the decorated samples was carried out using the Voigt Area G/L function to obtain three peaks centered at 450 nm (blue), 559 nm (green), and 673 nm (red).

Since Ca^{2+} is a stronger base than Ag^{+}, the interaction between the

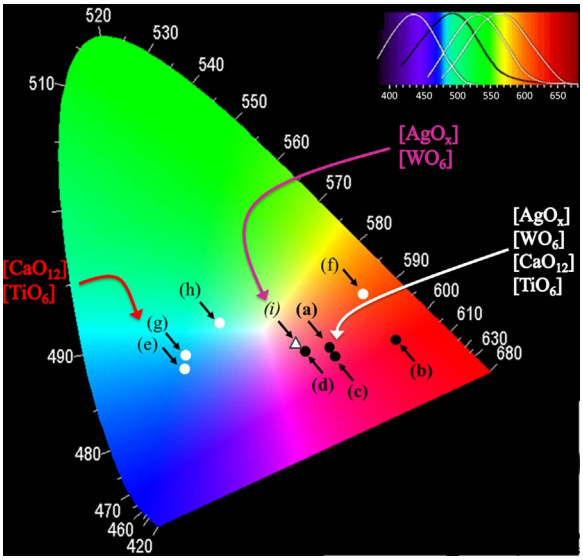

Fig. 10. CIE chromaticity diagram of (a) CT:AW4, (b) CT:AW8, (c) CT:AW16, (d) CT:AW32, (e) CT (4 min), (f) CT (8 min), (g) CT (16 min), (h) CT (32 min) and (*i*) AW. (For interpretation of the references to color in this figure, the reader is referred to the web version of this article.)

Table 1
CIE chromaticity coordinates x and y for the samples CT, AW and CT:AW.

Chromatic coordinate		
Samples	x	y
CT (4 min)	0.2151	0.2700
CT (8 min)	0.5180	0.3975
CT (16 min)	0.2165	0.2931
CT (32 min)	0.2738	0.3468
AW	0.4057	0.3111
CT:AW4	0.4619	0.3051
CT:AW8	0.5730	0.3181
CT:AW16	0.4705	0.2895
CT:AW32	0.4205	0.2991

AW clusters ($[AgO_x]/[WO_6]$) and the CT clusters ($[CaO_{12}]/[TiO_6]$) would result in the removal of Ag by Ca from the crystalline AW network. In this process, two Ag atoms and one O atom leave the network by forming Ag_2O, resulting in the formation of $[WO_4]$ that interacts with Ca^{2+} in order to form $CaWO_4$. The Ag and O vacancies are formed in the CT:AW samples (4 and 8 min) in which the bonding is not fully ordered in the long-range, thereby favoring the process. This is main responsible for the emission occurring in the red region 673 nm (1.84 eV).

The decorated CT:AW (4, 16, and 32 min) samples exhibit a strong emission in the blue region, at 450 nm (2.75 eV). However, the contact and sum of the both the emissions between the two semiconductor (CT and AW) favor a higher percentage of emission in the red region in the visible spectrum for all the decorated samples.

The CIE chromaticity diagram defining the colors of the samples is presented in Fig. 10. The pure CT samples exhibits a noticeable change in the color, which is influenced by varying the synthesis time that affects the distortion of $[CaO_{12}]$-$[TiO_6]$ clusters. The CT samples exhibit colors prospects of blue, cyan, and orange (Fig. 10(e)-(h)).

The PL spectra profile of AW indicates a broadband that covers the blue and red regions. Hence, AW exhibits a purplish pink color, in agreement with the literature (Fig. 10(*i*)) [44].

The PL spectra of the CT:AW samples indicate that the interactions between the $[AgO_x]/[WO_6]$-$[CaO_{12}]/[TiO_6]$ clusters favored emission in the red region, which can be observed from the chromaticity diagram. The colors of the decorated samples correspond to purplish pink to red (Fig. 10(a)-(d)). The chromaticity coordinates, x and y, of all the samples are given in Table 1.

In our model, the ideal photoluminescent crystal should exhibit some specific features. As noted in the previous analyses, our CT and AW crystals exhibit order–disorder structural defects ascribed to different types of distorted clusters $[TiO_6]_d$, $[CaO_{12}]_d$, $([WO_6]_d$, $[AgO_7]_d$, $[AgO_6]_d$, $[AgO_4]_d$, and $[AgO_2]_d$) as well as ordered clusters $[TiO_6]_o$, $[CaO_{12}]_o$, $([WO_6]_o$, $[AgO_7]_o$, $[AgO_6]_o$, $[AgO_4]_o$, and $[AgO_2]_o$). In addition, other characteristics, such as crystallographic preferred orientation, intermediary electronic levels, roughness, defects, and adsorption–desorption of decoration, are also important for properly analyzing the activity of different semiconductor crystals. Our CT and AW semiconductor samples exhibit the ability to generate electron and hole pairs. This characteristic can be attributed to the intrinsic defects present in the lattice of semiconductor materials having intermediary levels between the valence band and the conduction band, resulting in different PL properties and consequently different defect densities. Therefore, the presence of CT and AW in the crystals with different intermediate electronic levels, which consequently polarize the lattice, leads to different electronic transitions between ordered/distorted interfaces. The PL results show the variation AW defects in crystals, and CT as well as the influence caused at the interface. On the other hand, the study indicates that PL is a valuable tool for analyzing the interaction between semiconductors.

4. Conclusions

In summary, we have discussed the PL properties of the AW decorated CT samples prepared in this study. PL is favored in materials exhibiting structural disorders in the short, medium, and long ranges. The use of the MAH method resulted in the formation of CT samples with structural disorders. All the CT samples exhibited emission at room temperature owing to the presence of intermediate energy levels within the band gap since the emission wavelength was smaller than the experimentally obtained E_{gap} values. The PL spectra of CT samples showed an enhanced in the red emission part due the decorating with AW (CT:AW), since, an emission that covering the entire visible spectrum, with two maximum emissions (blue and red region), was achieved. This phenomenon is justified by interface effects inducing short-range defects in the $[TiO_6]$ clusters. The CIE chromaticity diagram indicates a favorable red-light emission for the samples.

Acknowledgements

The authors acknowledge the financial support of agencies: CAPES (PNPD – 1268069), FAPESP (2013/07296-2; 2013/26671-9), CNPq (304531/2013-8).

Appendix A. Supporting information

Supplementary data associated with this article can be found in the online version at http://dx.doi.org/10.1016/j.ceramint.2017.01.121.

References

[1] R. Gautam, P. Singh, S. Sharma, S. Kumari, A.S. Verma, Structural, electronic, optical, elastic and thermal properties of $CdGeP_2$ with the application in solar cell devices, Mater. Sci. Semicond. Process. 40 (2015) 727–736.
[2] C.-Y. Jin, O. Wada, Photonic switching devices based on semiconductor nano-structures, J. Phys. D: Appl. Phys. 47 (2014) 133001.
[3] K.J. Schmieder, A. Gerger, M. Diaz, Z. Pulwin, M. Curtin, L. Wang, C. Ebert, A. Lochtefeld, R.L. Opila, A. Barnett, GaAsP on SiGe/Si material quality improvements with in-situ stress sensor and resulting tandem device performance, Mater. Sci. Semicond. Process. 39 (2015) 614–620.
[4] G. Blasse, Luminescence of Inorganic Solids: from Isolated Centres to Concentrated Systems, Prog. Solid State Chem. 18 (1988) 79–171.
[5] S.K. Gupta, K. Sudarshan, P.S. Ghosh, S. Mukherjee, R.M. Kadam, Doping-Induced Room Temperature Stabilization of Metastable β-Ag_2WO_4 and Origin of Visible Emission in α- and β-Ag_2WO_4: low Temperature Photoluminescence Studies, J.

Phys. Chem. C. 120 (2016) 7265–7276.
[6] A. Alzahrani, A. Samokhvalov, Conventional and cryo-synchronous luminescence spectra of orthorhombic calcium titanate, J. Lumin. 178 (2016) 430–436.
[7] J. Li, Y.C. Zhang, T.X. Wang, M. Zhang, Low temperature synthesis and optical properties of $CaTiO_3$ nanoparticles from $Ca(NO_3)_2{\cdot}4H_2O$ and TiO_2 nanocrystals, Mater. Lett. 65 (2011) 1556–1558.
[8] E. Longo, D.P. Volanti, V.M. Longo, L. Gracia, I.C. Nogueira, M.A.P. Almeida, A.N. Pinheiro, M.M. Ferrer, L.S. Cavalcante, J. Andrés, Toward an understanding of the growth of Ag filaments on α-Ag_2WO_4 and their photoluminescent properties: a combined experimental and theoretical study, J. Phys. Chem. C 118 (2014) 1229–1239.
[9] G.F.G. Freitas, R.S. Nasar, M. Cerqueira, D.M.A. Melo, E. Longo, J.A. Varela, Luminescence in semi-crystalline zirconium titanate doped with lanthanum, Mater. Sci. Eng.: A 434 (2006) 19–22.
[10] F.M. Pontes, C.D. Pinheiro, E. Longo, E.R. Leite, S.R. de Lazaro, J.A. Varela, P.S. Pizani, T.M. Boschi, F. Lanciotti, The role of network modifiers in the creation of photoluminescence in $CaTiO_3$, Mater. Chem. Phys. 78 (2002) 227–233.
[11] A.T. De Figueiredo, S. De Lázaro, E. Longo, E.C. Paris, J.A. Varela, M.R. Joya, P.S. Pizani, Correlation among Order–Disorder, Electronic Levels, and Photoluminescence in Amorphous CT:Sm, Chem. Mater. 18 (2006) 2904–2911.
[12] B.J. Kennedy, C.J. Howard, B.C. Chakoumakos, Phase transitions in perovskite at elevated temperatures - a powder neutron diffraction study, J. Phys. Condens. Matter 11 (1999) 1479–1488.
[13] J. Milanez, A.T. de Figueiredo, S. de Lazaro, V.M. Longo, R. Erlo, V.R. Mastelaro, R.W.A. Franco, E. Longo, J.A. Varela, The role of oxygen vacancy in the photoluminescence property at room temperature of the $CaTiO_3$, J. Appl. Phys. 106 (2009) 043526.
[14] V.S. Marques, L.S. Cavalcante, J.C. Sczancoski, D.P. Volanti, J.W.M. Espinosa, M.R. Joya, M.R.M.C. Santos, P.S. Pizani, J.A. Varela, E. Longo, Influence of microwave energy on structural and photoluminescent behavior of $CaTiO_3$ powders, Solid State Sci. 10 (2008) 1056–1061.
[15] X. Qin, Y. Li, Y. Li, Y. Wu, R. Chen, K. Sharafudeen, Z. Ma, S. Liu, D. Wu, J. Qiu, Inducing NIR long persistent phosphorescence in Cr-doped perovskite titanate via redox, J. Alloy. Compd. 666 (2016) 387–391.
[16] G. Nag Bhargavi, A. Khare, Luminescence studies of perovskite structured titanates: a review, Opt. Spectrosc. 118 (2015) 902–917.
[17] T. Shimizu, Partial Oxidation of Hydrocarbons and Oxygenated Compounds on Perovskite Oxides, Catal. Rev. 34 (1992) 355–371.
[18] M.L. Moreira, E.C. Paris, G.S. do Nascimento, V.M. Longo, J.R. Sambrano, V.R. Mastelaro, M.I.B. Bernardi, J. Andrés, J.A. Varela, E. Longo, Structural and optical properties of $CaTiO_3$ perovskite-based materials obtained by microwave-assisted hydrothermal synthesis: an experimental and theoretical insight, Acta Mater. 57 (2009) 5174–5185.
[19] A.J. Vandenberg, C.A.H. Juffermans, The Polymorphism of Silver Tungstate Ag_2WO_4, J. Appl. Crystallogr. 15 (1982) 114–116.
[20] J. Andres, L. Gracia, P. Gonzalez-Navarrete, V.M. Longo, W. Avansi Jr., D.P. Volanti, M.M. Ferrer, P.S. Lemos, F.A. La Porta, A.C. Hernandes, E. Longo, Structural and electronic analysis of the atomic scale nucleation of Ag on α-Ag_2WO_4 induced by electron irradiation, Sci. Rep. 4 (2014) 5391.
[21] Z. Lin, J. Li, Z. Zheng, J. Yan, P. Liu, C. Wang, G. Yang, Electronic Reconstruction of α-Ag_2WO_4 Nanorods for Visible-Light Photocatalysis, ACS Nano 9 (2015) 7256–7265.
[22] Y.F. Chen, S.R. Sheen, Coprecipitation Synthesis of a Superconductor Via Multi-precipitants, J. Chin. Chem. Soc. 47 (2000) 307–314.
[23] Y. Ma, E. Vileno, S.L. Suib, P.K. Dutta, Synthesis of Tetragonal $BaTiO_3$ by Microwave Heating and Conventional Heating, Chem. Mater. 9 (1997) 3023–3031.
[24] W. Sun, J. Li, W. Liu, C. Li, Preparation of Fine Tetragonal Barium Titanate Powder by a Microwave-Hydrothermal Process, J. Am. Ceram. Soc. 89 (2006) 118–123.
[25] T.M. Mazzo, I.M. Pinatti, L.R. Macario, W. Avansi, M.L. Moreira, I.L.V. Rosa, V.R. Mastelaro, J.A. Varela, E. Longo, Europium-doped calcium titanate: optical and structural evaluations, J. Alloy. Compd. 585 (2014) 154–162.
[26] Y.V.B. De Santana, J.E.C. Gomes, L. Matos, G.H. Cruvinel, A. Perrin, C. Perrin, J. Andres, J.A. Varela, E. Longo, Silver Molybdate and Silver Tungstate Nanocomposites with Enhanced Photoluminescence, Nanomater. Nanotechnol. 4 (2014) 22.
[27] S. Sasaki, C.T. Prewitt, J.D. Bass, W.A. Schulze, Orthorhombic Perovskite $CaTiO_3$ and $CdTiO_3$: structure ans Space Group, Acta Crystallogr. Sect. C. - Struct. Chem. 43 (1987) 1668–1674.
[28] L.S. Cavalcante, V.S. Marques, J.C. Sczancoski, M.T. Escote, M.R. Joya, J.A. Varela, M.R.M.C. Santos, P.S. Pizani, E. Longo, Synthesis, structural refinement and optical behavior of $CaTiO_3$ powders: a comparative study of processing in different furnaces, Chem. Eng. J. 143 (2008) 299–307.
[29] U. Balachandran, N.G. Eror, Laser-induced Raman scattering in calcium titanate, Solid State Commun. 44 (1982) 815–818.
[30] T. Hirata, K. Ishioka, M. Kitajima, Vibrational Spectroscopy and X-Ray Diffraction of Perovskite Compounds $Sr_{1-x}M_xTiO_3$ (M = Ca, Mg; 0≤ x≤1), J. Solid State Chem. 124 (1996) 353–359.
[31] I.G. Siny, R.W. Tao, R.S. Katiyar, R.A. Guo, A.S. Bhalla, Raman Spectroscopy of Mg-Ta order-disorder in $BaMg_{1/3}Ta_{2/3}O_3$, J. Phys. Chem. Solids 59 (1998) 181–195.
[32] H. Zheng, I.M. Reaney, G.D.C. Csete de Gyorgyfalva, Raman spectroscopy of $CaTiO_3$-based perovskite solid solutions, J. Mater. Res. 19 (2004) 488–495.
[33] P.M. Skarstad, S. Geller, $(W_4O_{16})^{8-}$ Polyion in high temperature modification of silver tungstate, Mater. Res. Bull. 10 (1975) 791–799.
[34] A. Turkovic, D.L. Fox, J.F. Scott, S. Geller, G.F. Ruse, High-Temperature Raman Spectroscopy of Silver TetraTungstate, $Ag_8W_4O_{16}$, Mater. Res. Bull. 12 (1977) 189–196.
[35] T.J. Yan, L.P. Li, W.M. Tong, J. Zheng, Y.J. Wang, G.S.J. Li, Solid State Chem. 184 (2011) 357–364.
[36] M.I. Kay, B.C. Frazer, I. Almodovar, Neutron Diffraction Refinement of $CaWO_4$, J. Chem. Phys. 40 (1964) 504–506.
[37] A. Taoufyq, F. Guinneton, J.C. Valmalette, M. Arab, A. Benlhachemi, B. Bakiz, S. Villain, A. Lyoussi, G. Nolibe, J.R. Gavarri, Structural, vibrational and luminescence properties of the (1–x)$CaWO_4$–x$CdWO_4$ system, J. Solid State Chem. 219 (2014) 127–137.
[38] P. Kubelka, F. Munk, Ein Beitrag zur Optik der Farbanstriche, Zeit Für Tech. 12 (1931) 593–601.
[39] D.L. Wood, J. Tauc, Weak absorption tails in amorphous semiconductors, Phys. Rev. B 5 (1972) 3144–3151.
[40] R.A. Roca, J.C. Sczancoski, I.C. Nogueira, M.T. Fabbro, H.C. Alves, L. Gracia, L.P.S. Santos, C.P. de Sousa, J. Andrés, G.E. Luz, E. Longo, L.S. Cavalcante, Facet-dependent photocatalytic and antibacterial properties of α-Ag_2WO_4 crystals: combining experimental data and theoretical insights, Catal. Sci. Technol. 5 (2015) 4091–4107.
[41] V.M. Longo, L.S. Cavalcante, R. Erlo, V.R. Mastelaro, A.T. de Figueiredo, J.R. Sambrano, S. de Lázaro, A.Z. Freitas, L. Gomes, N.D. Vieira, J.A. Varela, E. Longo, Strong violet–blue light photoluminescence emission at room temperature in $SrZrO_3$: joint experimental and theoretical study, Acta Mater. 56 (2008) 2191–2202.
[42] L.S. Cavalcante, M.A. Almeida, W. Avansi Jr., R.L. Tranquilin, E. Longo, N.C. Batista, V.R. Mastelaro, M.S. Li, Cluster coordination and photoluminescence properties of α-Ag_2WO_4 microcrystals, Inorg. Chem. 51 (2012) 10675–10687.
[43] M. Tyagi, Sangeeta, S.C. Sabharwal, Luminescence properties of $BaWO_4$ single crystal, J. Lumin. 128 (2008) 1528–1532.
[44] I.M. Pinatti, I.C. Nogueira, W.S. Pereira, P.F. Pereira, R.F. Goncalves, J.A. Varela, E. Longo, I.L. Rosa, Structural and photoluminescence properties of Eu^{3+} doped α-Ag_2WO_4 synthesized by the green coprecipitation methodology, Dalton Trans. 44 (2015) 17673–17685.